2024 International Conference on Simulation of Semiconductor Processes and Devices (SISPAD) | 979-8-3315-1635-2/24/$31.00 ©2024 IEEE | DOI: 10.1109/SISPAD62626.2024.10732911

Towards Low Contact Resistance Metal Transition-Metal Dichalcogenide Contacts – A Quantum Transport Study

Pranay Baikadi[1,a], Raseong Kim[2,b], Peter Reyntjens[1,3,4,c], Ashish Verma Penumatcha[2,d], Maarten Van de Put [4,e], and William G. Vandenberghe[1,f]

[1]*Dept. of Materials Science and Engineering, The University of Texas at Dallas,* Dallas, USA.
[2]*Components Research, Intel Corporation,* Hillsboro, USA.
[3]*Dept. of Material Engineering, KU Leuven,* Leuven, Belgium.
[4]*imec,* Leuven, Belgium.
Email: [a]pxb210000@utdallas.edu, [b]raseong.kim@intel.com, [c]pdr180000@utdallas.edu, [d]ashish.verma.penumatcha@intel.com, [e]maarten.vandeput@imec.be, [f]wxv101020@utdallas.edu.

***Abstract*—In this study, we use Non-Equilibrium Green's Function (NEGF) based quantum transport simulations to investigate metal-Transition Metal Dichalcogenide (TMD) top contacted geometries. Using MoS_2 as an example TMD, we explore the impact of the surrounding dielectric environment and spatially non-uniform doping in MoS_2 on contact resistance. We find that a low permittivity top dielectric is crucial in reducing the tunneling width for electrons and thus contact resistance. We also find that heavily doping the MoS_2 monolayer underneath the metal has an insignificant effect in terms of reducing the tunneling width and contact resistance whereas the doping in the channel region is critical.**

***Keywords*—quantum transport, top contacts, Transition-Metal Dichalcogenide, contact resistance, doping, dielectric environment**

I. INTRODUCTION

Transition-Metal Dichalcogenides (TMDs) are atomically flat, layered compounds with a chemical formula of MX_2 (M = Mo, W or Nb and X = S, Se or Te) [1]. The presence of a bandgap (E_g) in several TMDs [2], lack of dangling bonds that give rise to interface states in the bandgap, phonon-limited electron mobility of $\sim 183\,\mathrm{cm}^2\mathrm{V}^{-1}\mathrm{s}^{-1}$ [3] and superior electrostatic control due to the large surface-to-volume ratio, make TMDs suitable as the channel material in the next generation transistors [4]. However, metal contacts to the TMDs, an integral part of any transistor architecture, are characterized by strong Fermi level pinning (FLP) with large contact resistance (R_C) and poor ON current [5]. Even with ultra-clean interfaces, the penetration of metal induced gap states (MIGS) into the TMD bandgap results in the Fermi level being pinned to the branch-point energy [6].

An interesting approach reported recently is the use of semi-metals such as Bismuth (Bi), Antimony (Sb) and Tin (Sn) to contact the TMD, utilizing the low density of states at the Fermi level of semi-metals to de-pin the Fermi level [7-9]. Alternatively, others have shown that MIGS can also be reduced by introducing buffer layers such as h-BN between the metal and the TMD [10]. However, the relatively low melting points of materials such as Bi and Sn [11] and the inherent complexity in fabrication introduced by buffer layers, make these approaches incompatible with the current complementary metal-oxide semiconductor (CMOS) process flow.

In this work, we use our in-house transport solver [12, 13] to model metal-monolayer MoS_2 (1L-MoS_2) top contacted geometry by solving the single particle, effective mass Schrodinger equation under the quantum transmitting boundary method (QTBM) formalism [14]. We investigate the effect of the surrounding dielectric environment, spatially non-uniform doping in the 1L-MoS_2, while accounting for the image force barrier lowering (IFBL) effect. This paper is organized as follows: We first describe the methodology used in this work to calculate transmission probabilities and R_C. Next, we present our results by comparing the potential profiles, current density cutlines and electric field profiles for different dielectric setups and doping profiles. Lastly, we draw conclusions identifying the best dielectric setup and doping profile to reduce R_C.

II. METHODOLOGY

Our approach to calculate R_C can be broadly divided into three steps, as shown in Fig. 1a. In the first step, the top contacted heterostructure is created starting from a unit cell of dimensions $L_x = 2.86$ Å, $L_y = 4.96$ Å, and $L_z = 62.3$ Å, consisting of a monolayer of MoS_2 and two metal layers (shown in red), separated by an interlayer distance (d_i) of 2.5 Å as depicted in Fig. 1b. In order to prevent any unphysical coupling between the unit cell and its neighboring periodic images along the z-direction, we add 24.3 Å of vacuum above the top metal layer and 28 Å of vacuum below the 1L-MoS_2. A crucial step here is to calculate the eigenstates of the unit cell $u_{nk}(\boldsymbol{r})$, necessary to construct the Bloch basis. The unit cell is repeated periodically as discrete finite element (FE) blocks along the transport direction, x, up to a desired length (L_dev). To create the top contact heterostructure with an overlap length L_ov, some metal atoms above the 1L-MoS_2 need to be eliminated. This is accomplished by summing up the potential profiles of all the metal atoms to be removed $(V_\mathrm{rem}(\boldsymbol{r}))$, and applying the negative of this potential, i.e., $-V_\mathrm{rem}(\boldsymbol{r})$ to the entire simulation domain, as shown in Fig. 1c.

In terms of materials modeling, the metal atoms in the unit cell are modeled using atomistic empirical pseudopotentials with an energy cut-off of 250 eV. The three atoms in the 1L-MoS_2 however, are modeled in a continuum description using the local potential of 1L-MoS_2 extracted from the Vienna *Ab-initio* Simulation Package (VASP) [15]. The three dimensional local potential is $x - y$ averaged, yielding a potential that varies

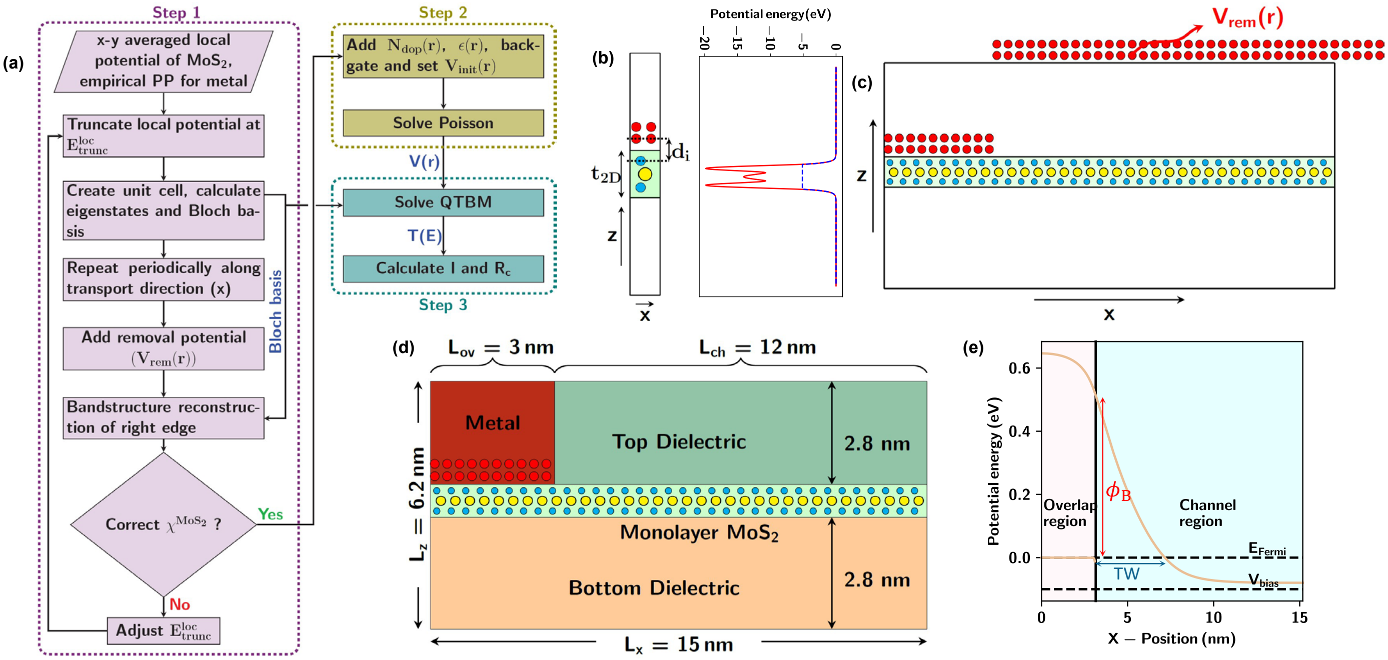

Fig. 1 (a) Flow chart of our simulation methodology consisting of three steps. $V_{IFBL}(\boldsymbol{r})$ is calculated analytically and the combined potential $V(\boldsymbol{r})+V_{IFBL}(\boldsymbol{r})$ is given as input to the transport kernel. (b) Cartoon of the unit cell used in our calculations, where the red, blue and yellow circles indicate the metal, sulfur (S) and molybdenum (Mo) atoms respectively. (c) Removal potential $V_{rem}(\boldsymbol{r})$ is added to the simulation domain to eliminate some atoms above the 1L-MoS$_2$. (d) Schematic of the top contact heterostructure used in our simulations. (e) An example band-diagram depicting the definitions of the Schottky barrier height (ϕ_B) and the tunneling width (TW).

only along the z-direction. Depending on the electron affinity of the TMD (χ_{TMD}), the averaged local potential is truncated at $E_{\text{trunc}}^{\text{loc}}$. This is determined iteratively, by comparing the electron affinity obtained from the band structure of the rightmost finite element block, consisting of only the TMD, and the experimental electron affinity of the free standing TMD. For the case of 1L-MoS$_2$ with $\chi_{\text{MoS}_2} = 4.27$ eV [2], $E_{\text{trunc}}^{\text{loc}} = -5.13$ eV yields the correct affinity of the 1L-MoS$_2$.

In the second step of our methodology, we solve the Poisson equation given by

$$\nabla\cdot\big(\epsilon(\boldsymbol{r})\cdot\nabla V(\boldsymbol{r})\big) = \rho_{\text{free}}(\boldsymbol{r},V) + \rho_{\text{doping}}(\boldsymbol{r}), \qquad (1)$$

where $V(\boldsymbol{r})$ is the Hartree potential, $\rho_{\text{free}}(\boldsymbol{r},V)$ is the electron charge density, $\rho_{\text{doping}}(\boldsymbol{r})$ is the non-electrostatic doping and $\epsilon(\boldsymbol{r})$ is the relative permittivity tensor. For the 1L-MoS$_2$, the in-and-out-of-plane dielectric constants are taken from [16], while the permittivities for the top and the bottom dielectrics are taken from [17]. The electron charge density in the metal $\left(\rho_{\text{free}}^{\text{met}}(\boldsymbol{r})\right)$ and the 1L-MoS$_2$ $(\rho_{\text{free}}^{\text{MoS}_2})$ are modeled semiclassically as

$$\rho_{\text{free}}^{\text{met}}(\boldsymbol{r}) = DOS_{\text{met}} \times (qV(\boldsymbol{r}) - \phi_{\text{met}}) \qquad (2)$$

and $$\rho_{\text{free}}^{\text{MoS}_2} = \frac{2m^* k_{\text{B}}T}{t_{\text{2D}}\pi\hbar^2}\ln\left(1+e^{-\left(\frac{qV(r)-\chi_{\text{MoS}_2}-\mu_{\text{R}}}{k_{\text{B}}T}\right)}\right), \qquad (3)$$

where DOS_{met} is the density of states of bulk metal at the Fermi level, q is the elementary charge, k_{B} is the Boltzmann constant, T is the temperature, μ_{R} is the chemical potential of the right reservoir set to -0.1 eV, $\hbar$ is the reduced Planck's constant, $m^* = \sqrt{m_{xx}m_{yy}}$ is the electron effective mass and t_{2D} is the thickness of the 1L-MoS$_2$ at 6.12 Å [17]. Neumann boundary conditions are applied at all the boundaries, and (1) is solved on a FE mesh using the algebraic multigrid method. The self-consistent potential from the Poisson equation is added to the IFBL potential, calculated separately using the analytical expression provided in [18], and the conduction band diagrams are extracted as shown in Fig. 1e. The combined potential is used in constructing the Hamiltonian matrix $\mathcal{H}$ in the transport kernel described below.

In the last step, we solve the device level Schrödinger equation under the QTBM formalism. Firstly, the full device wavefunction $\Psi_{ink}(\boldsymbol{r})$ is expanded in terms of the eigenstates of the unit cell and the FE shape functions $f_i(\boldsymbol{r})$ as

$$\Psi_{ink}(\boldsymbol{r}) = \sum_{ink} c_{ink} f_i(\boldsymbol{r}) u_{nk}(\boldsymbol{r}) e^{\text{i}k(x-x_i)}, \qquad (4)$$

where c_{ink} are the expansion coefficients to be evaluated. The device level Schrödinger equation is converted into the weak variational form using $\Psi_{ink}^*(\boldsymbol{r})$ as the FE test functions, from which $\mathcal{H}$ is constructed. Assuming open boundary conditions, the collection of states at an energy E to be injected into the simulation domain is obtained from the complex bandstructure of the left and the right leads, which are extensions of the first and the last FE blocks. The resulting matrix equation is

$$[\mathcal{H} - E\text{M}]\mathbf{c} = \text{B}(E), \qquad (5)$$

where B is the source matrix, with the columns describing the states of energy E being injected, M is the overlap matrix resulting from the FE discretization and $\mathbf{c}$ is the expansion coefficients to be calculated. Equation (5) is solved for a collection of energies E, and the real space wavefunctions are calculated from $\mathbf{c}$ using (4), from which the transmission coefficients $\text{T}(E)$ are evaluated. The current through the contact is calculated as

$$I = \frac{q}{\pi\hbar}\int \mathrm{d}k_y \int \mathrm{d}E\, T(E,k_y)\big(f_{\text{L}}(E,\mu_{\text{L}}) - f_{\text{R}}(E,\mu_{\text{R}})\big), \qquad (6)$$

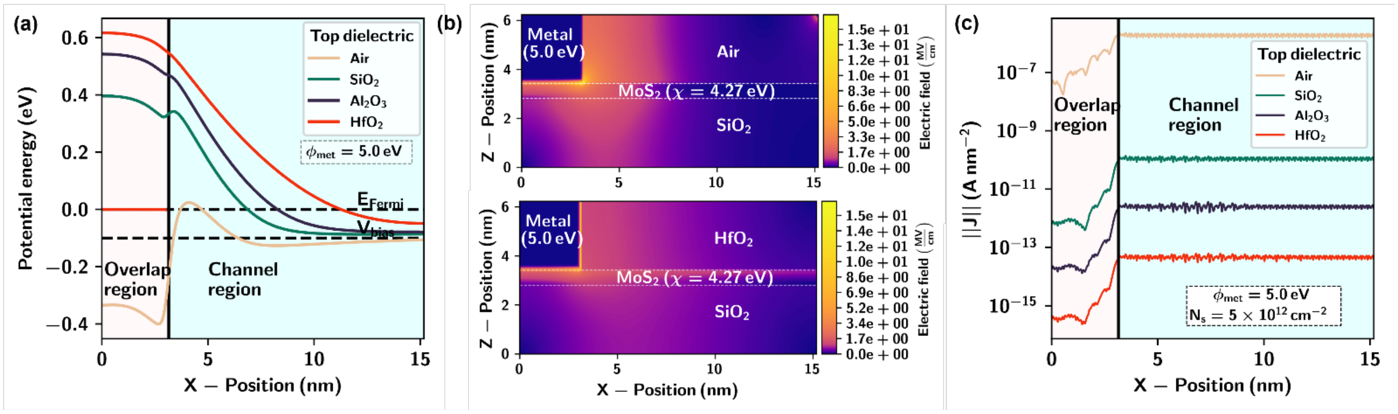

Fig. 2 Effect of the surrounding dielectric environment. (a) Band-diagrams as a function of the permittivity of the top dielectric. (b) Comparison of the electric field between the top Air/bottom SiO_2 and top HfO_2/bottom SiO_2 dielectric setups. (c) Cutlines of magnitude of current density at the center of the 1L-MoS_2 for the four choices of the top dielectric.

where $f_{\rm L(R)}$ and $\mu_{\rm L(R)}$ are the Fermi-Dirac distribution and the chemical potential of the left (right) lead. $R_{\rm C}$ is calculated using the Ohm's law as $R_{\rm C} = \frac{V_{\rm bias}}{I}$, where $V_{\rm bias}$ is the bias of 0.1 V (or -0.1 eV) applied to the right lead.

III. RESULTS

A. *Effect of the surrounding dielectric*

In Fig. 2a we compare the conduction band diagrams as a function of four choices of the top dielectric. The bottom dielectric is taken to be SiO_2, the 1L-MoS_2 is uniformly n-doped to $N_s = 5\times10^{12}\rm cm^{-2}$ and the workfunction of the metal ($\phi_{\rm met}$) is taken to be 5.0 eV. As the relative permittivity of the top dielectric is reduced from HfO_2 to Air, we see that the TW reduces gradually. We also see that the barrier lowering effect is particularly significant when considering low-κ dielectrics, as the barrier lowering is inversely proportional to the permittivity of the surrounding dielectric.

Fig. 2b compares the color plots of the magnitude of the electric field inside the simulation domain between the top Air/bottom SiO_2 and top HfO_2/bottom SiO_2 dielectric setups. The electric field in the region next to the right edge of the metal is higher in the top Air/bottom SiO_2 compared to the top HfO_2/bottom SiO_2 setup. Since a high-κ dielectric such as HfO_2 is more polarizable, the electric field from the metal is greatly screened, reducing the strength of the net electric field. A lower net electric field then translates to a larger TW and high $R_{\rm C}$.

In Fig. 2c we show the cutlines of the magnitude of current density along the length of the 1L-MoS_2 for the four dielectric setups. The current density inside the monolayer increases as the permittivity of the top dielectric is reduced, with ~5 orders of magnitude improvement in the current density from top HfO_2/bottom SiO_2 to top Air/bottom SiO_2 dielectric setups. It is also interesting to note that the current density in the portion of the 1L-MoS_2 underneath the contacting metal, i.e., from 0 nm to 3 nm, is nearly 2 orders of magnitude lower than the rest of the 1L-MoS_2, since barrier height seen by the electrons moving from the metal into the 1L-MoS_2 is the lowest at the right edge of the metal. Therefore, using a low-κ top dielectric can greatly improve $R_{\rm C}$ at the metal-MoS_2 interface by lowering the TW and increasing the contribution of the tunneling current.

B. *Effect of non-uniform doping*

In Fig. 3 we explore the effect of spatially non-uniform doping in the 1L-MoS_2. The monolayer is divided into the overlap and the channel regions, depicted as blue and green rectangles in the inset of Fig. 3a. Here we plot $R_{\rm C}$ as a function of the doping in the channel region $\left(N_{\rm s}^{\rm ch}\right)$ for five different values of the overlap doping ($N_{\rm s}^{\rm ov}$). We see that $R_{\rm C}$ decreases by ~7 orders of magnitude as $N_{\rm s}^{\rm ch}$ is increased from $1\times10^{12}\,\rm cm^{-2}$ to $1\times10^{13}\,\rm cm^{-2}$. The same increase in $N_{\rm s}^{\rm ov}$ however has an insignificant effect in reducing $R_{\rm C}$, for any given choice of $N_{\rm s}^{\rm ch}$. This is in sharp contrast to the expectation that heavily doping the semiconductor close to the metal improves $R_{\rm C}$ by reducing TW.

Fig. 3b shows a 3D color plot of the calculated TWs as a function of $N_{\rm s}^{\rm ch}$ and $N_{\rm s}^{\rm ov}$. We see that increasing $N_{\rm s}^{\rm ch}$ by one order of magnitude results in ~6x reduction in TW, while the same increase in $N_{\rm s}^{\rm ov}$ has virtually no effect in terms of reducing TW. This is consistent with the trends in $R_{\rm C}$ observed in Fig. 3a.

Fig. 3c provides an explanation by comparing the band-diagrams for four doping profiles in the 1L-MoS_2. As expected, the TW is the largest for case where the monolayer is undoped (solid red). As $N_{\rm s}^{\rm ov}$ is increased to $1\times10^{13}\rm cm^{-2}$ with $N_{\rm s}^{\rm ch} = 0\,\rm cm^{-2}$ (dotted red), we do not see a significant reduction in TW. In contrast, if $N_{\rm s}^{\rm ch}$ is increased to $1\times10^{13}\rm cm^{-2}$ with $N_{\rm s}^{\rm ov} = 0\,\rm cm^{-2}$ (dotted green), we see a drastic reduction TW. Further increase in doping in the overlap region has an insignificant effect in reducing $R_{\rm C}$ (solid green). Therefore, doping level in the overlap region has an insignificant effect in reducing $R_{\rm C}$, while doping the channel region heavily reduces the TW and therefore $R_{\rm C}$. This conclusion is not entirely surprising considering the thickness of the 1L-MoS_2. Since the monolayer is merely 6.12 Å thick, the region underneath the metal remains depleted in spite of heavy doping. A similar conclusion has been reached in the work of Arutchelvan et al. [19] using a semiclassical TCAD based study on transport mechanisms in metal-MoS_2 contacts.

CONCLUSIONS

Quantum transport simulations are performed on top contacted 1L-MoS_2 to investigate the impact of surrounding

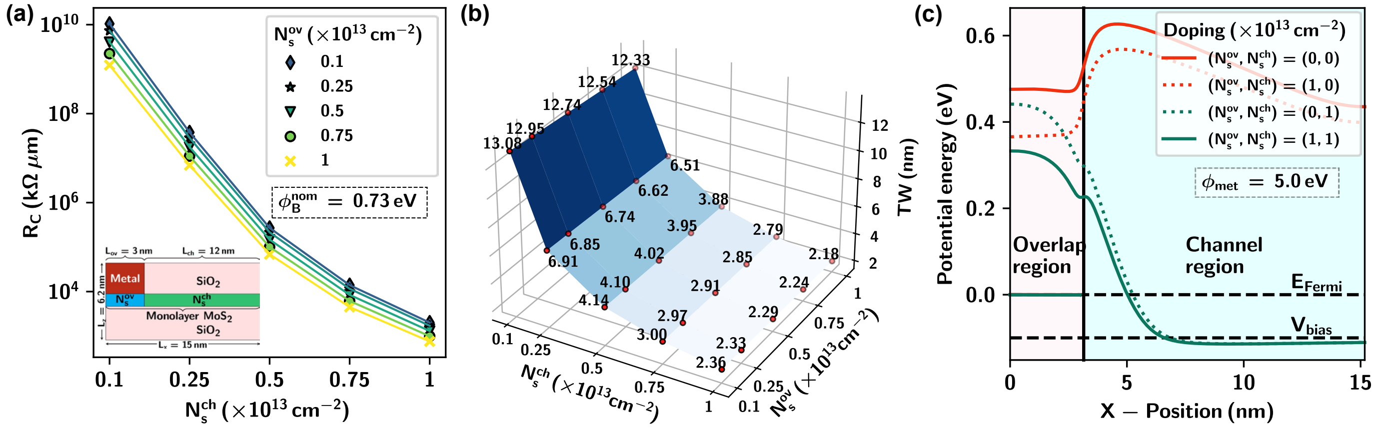

Fig. 3 Effect of spatially non-uniform doping in 1L-MoS$_2$. (a) R_C as a function of doping level (N_S^{ch}) in the channel region (green rectangle in the inset) for different levels of doping (N_S^{ov}) in the overlap region (blue rectangle in the inset). (b) TW as a function of N_S^{ch} and N_S^{ov}. (c) Comparison of conduction band-diagrams for four doping profiles in 1L-MoS$_2$.

dielectric environment and spatially non-uniform doping on R_C. We see that a low- κ dielectric makes two important contributions in reducing R_C – by reducing the TW for electrons to tunnel into the TMD from the metal and enhancing the barrier lowering effect at the metal-MoS$_2$ interface. In terms of doping, we find that the level of doping in the region of the 1L-MoS$_2$ underneath the metal (N_s^ov) has an insignificant effect in reducing R_C. TW is found to strongly depend on N_s^ch, decreasing by a factor of 6 for an order of increase in N_s^ch from 1×10^{12} cm^{-2} to 1×10^{13} cm^{-2}.

ACKNOWLEDGMENT

This material is based upon work supported by Intel Corporation. We acknowledge the Texas Advanced Computing Center at The University of Texas at Austin for providing high performance computing resources.

REFERENCES

[1] Geim, A., Grigorieva, I. Van der Waals heterostructures. *Nature* 499, 419–425 (2013).

[2] C. Zhang *et al.*, "Systematic study of electronic structure and band alignment of monolayer transition metal dichalcogenides in Van der Waals heterostructures," *2D Mater.*, vol. 4, no. 1, p. 015026, Nov. 2016.

[3] L.Cheng, C. Zhang, and Y. Liu, "Why two-dimensional semiconductors generally have low electron mobility," Physical Review Letters, vol. 125, no. 17, p. 177701, 2020.

[4] Das, S. *et al.* Transistors based on two-dimensional materials for future integrated circuits. *Nat Electron* **4**, 786–799 (2021).

[5] Y. Zheng, J. Gao, C. Han, and W. Chen, "Ohmic Contact Engineering for Two-Dimensional Materials," *Cell Reports Physical Science*, vol. 2, no. 1, p. 100298, Jan. 2021.

[6] K. Sotthewes *et al.*, "Universal Fermi-Level Pinning in Transition-Metal Dichalcogenides," *J. Phys. Chem. C*, vol. 123, no. 9, pp. 5411–5420, Mar. 2019.

[7] P.-C. Shen *et al.*, "Ultralow contact resistance between semimetal and monolayer semiconductors," *Nature*, vol. 593, no. 7858, pp. 211–217, May 2021.

[8] K. P. O'Brien *et al.*, "Advancing 2D Monolayer CMOS Through Contact, Channel and Interface Engineering," in *2021 IEEE International Electron Devices Meeting (IEDM)*, Dec. 2021, p. 7.1.1-7.1.4.

[9] A.-S. Chou *et al.*, "High On-State Current in Chemical Vapor Deposited Monolayer MoS2 nFETs With Sn Ohmic Contacts," *IEEE Electron Device Letters*, vol. 42, no. 2, pp. 272–275, Feb. 2021.

[10] K. Andrews, A. Bowman, U. Rijal, P.-Y. Chen, and Z. Zhou, "Improved Contacts and Device Performance in MoS2 Transistors Using a 2D Semiconductor Interlayer," *ACS Nano*, vol. 14, no. 5, pp. 6232–6241, May 2020.

[11] https://www.engineeringtoolbox.com/meltingpoints-mixtures-metals-d_1269.html.

[12] M. L. Van de Put, M. V. Fischetti, and W. G. Vandenberghe, "Scalable atomistic simulations of quantum electron transport using empirical pseudopotentials," *Computer Physics Communications*, vol. 244, pp. 156–169, Nov. 2019.

[13] M. Van de Put, "PETRA." https://gitlab.com/petra-sim/petra.

[14] C. S. Lent and D. J. Kirkner, "The quantum transmitting boundary method," *Journal of Applied Physics*, vol. 67, no. 10, pp. 6353–6359, May 1990.

[15] G. Kresse and J. Hafner, "Ab initio molecular dynamics for liquid metals," Physical review B, vol. 47, no. 1, p. 558, 1993.

[16] A. Laturia, M. L. Van de Put, and W. G. Vandenberghe, "Dielectric properties of hexagonal boron nitride and transition metal dichalcogenides: from monolayer to bulk," *npj 2D Mater Appl*, vol. 2, no. 1, p. 6, Dec. 2018.

[17] J. Robertson, "High dielectric constant oxides," The European Physical Journal-Applied Physics, vol. 28, no. 3, pp. 265–291, 2004.

[18] S. R. Evans, E. Deylgat, E. Chen, and W. G. Vandenberghe, "Image-force barrier lowering of schottky barriers in two-dimensional materials as a function of metal contact angle," Physical Review Applied, vol. 20, no. 4,p. 044003, 2023.

[19] G. Arutchelvan *et al.*, "From the metal to the channel: a study of carrier injection through the metal/2D MoS $_2$ interface," *Nanoscale*, vol. 9, no. 30, pp. 10869–10879, 2017.